



Article submitted to journal

Subject Areas:

Mechanics, Applied mathematics

Keywords:

Rolling friction, granular media, plasticity

Author for correspondence:

Keaton J. Burns

[e-mail: kjburns@mit.edu](mailto:kjburns@mit.edu)

Rolling resistance of shallow granular deformation

Keaton J. Burns¹, Neil J. Balmforth², and Ian J. Hewitt³

¹Department of Physics, Massachusetts Institute of Technology, Cambridge, MA, 02139, U.S.

²Department of Mathematics, University of British Columbia, 1984 Mathematics Road, Vancouver, BC, V6T 1Z2, Canada

³Mathematical Institute, University of Oxford, OX2 6GG, U.K.

Experiments are conducted to measure the resistance experienced by light cylinders rolling over flat beds of granular media. Sand and glass spheres are used for the beds. The trajectories of the rolling cylinders are determined through optical tracking, and velocity and acceleration data are inferred through fits to these trajectories. The rolling resistance is dominated by a velocity-independent component, but a velocity dependent drag exceeding the expected strength of air drag is also observed. The results are compared to a theoretical model based on a cohesionless Mohr-Coulomb rheology for a granular medium in the presence of gravity. The model idealises the flow pattern underneath the rolling cylinder as a plastically deforming zone in front of a rigidly rotating plug attached to the cylinder, as proposed previously for cylinders rolling on perfectly cohesive plastic media. The leading-order, rate-independent rolling resistance observed experimentally is well reproduced by the model predictions.

1. Introduction

It is commonly experienced that motion over loose sand is hindered by the response of the granular medium to the applied load. In particular, sandy surfaces often present substantial difficulties to wheeled vehicles [1], impacting the design of tires and robotic rovers [2,3]. The rolling of rocks over sand may also play an important role in geophysical processes such as the formation of screes [4]. Although Coulomb provided detailed measurements of rolling resistance, Reynolds [5] gave the first quantitative discussion of the origin of the phenomenon in terms of the deformation of the surface in rolling contact. The resulting friction experienced by rubber and metal surfaces is now understood to be a combination of Reynolds' deformation and surface adhesion [6,7]. For wheels travelling over sand, the problem is complicated further by the lack of a general theory of the deformation of a granular medium, the significant depth to which the wheels of a heavy vehicle will sink, and the substantial sideways flow of sand. Nevertheless, a rich vein of literature has built up on the resistance to wheels driven over sand and soft soils (e.g. [1,3,8–16]).

In this work, we consider the rolling motion of a long and light cylinder over an initially static granular bed. In this limit, the contact area between the cylinder and the bed is small relative to the surface area of the cylinder, and the deformation of the granular media is largely two-dimensional and both localised and superficial. This sets our work apart from much of the literature on rotating wheels and recent experiments on rolling spheres [17], where the problem is inherently three-dimensional and the weight of the object traversing the surface leads to significant sinking and compaction of the underlying granular material. Additional complications are thereby minimised, which may allow us to gain better insight into the dynamics of granular deformation under a rolling object.

Our study begins with a series of experiments to determine the resistance experienced by the rolling cylinders. A particular focus is to experimentally examine the dependence of the resistance on the speed of the cylinders, which reflects the rate-dependent rheology of the granular material and bears on the relevance of recently proposed empirical friction laws [18]. For this task, we use two types of granular media: a coarse sand and glass spheres (ballotini). For both, the grain size is much smaller than the radii of the rolling cylinders.

We complement the experiments with a rate-independent theoretical model for the leading-order resistance based on Mohr-Coulomb plasticity theory for the granular bed. In the limit that the contact area is much smaller than the cylinder area, the stress field induced by the rolling cylinder can be constructed by asymptotic theory. This device, which was proposed by Spencer [19,20], has been used previously to model the rolling of cylinders over cohesive material [21,22], neglecting the effect of gravity. For a non-cohesive granular medium with a free surface, however, gravity cannot be neglected, as in the calculation of the critical load supported by a foundation [23–25]. Our analysis applies Spencer's method to a cylinder rolling over such materials.

A critical detail of the generalisation is the flow pattern that must be adopted underneath the contact region between the sand and cylinder. We adopt a construct proposed by Collins [26] (see also [27]) in which the deformation due to rolling consists of two parts: a zone of plastic deformation extending below and ahead of the forward section of the contact region, together with a plug that is rigidly attached to the cylinder below the rear section of the contact region. Collins' construction allows for contacts that are not necessarily small and has received some support from numerical computations [15], but was proposed for cohesive material neglecting gravity. The two-part structure of the flow pattern is, however, essential for a consistent description of the forces and torques acting on the cylinder, and is reminiscent of experiments and models of wheels rolling over sand [9–14].

The experimental apparatus, procedures, and dataset are described in § 2. In § 3, we outline the theoretical model to calculate rolling resistance. We compare the predictions of the model to our experimental results in § 4. The Appendices contain some additional theoretical results, exposing

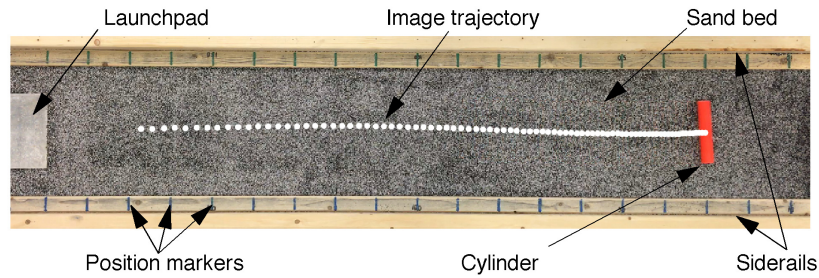


Figure 1: Channel geometry: final frame of a rolling cylinder trial on the sand bed with the corresponding image trajectory plotted in white.

Material	d (mm)	ρ_s (g/cm ³)	ϕ_c (deg)
Aquarium sand	0.9 ± 0.15	1.59 ± 0.09	36.1 ± 1.0
Ballotini	1.0 ± 0.2	1.55 ± 0.07	23.7 ± 0.6

Table 1: Mean particle diameter d , apparent density ρ_s , and dynamic angle of repose ϕ_c of the granular media used in the experiments [28].

issues with the Mohr-Coulomb predictions for the velocity field and free surface of the granular medium, and relating our analysis back to that of Collins [26].

2. Experiments

(a) Apparatus and protocol

We constructed a channel using a high-density polyethylene board and wooden side-rails to contain a bed of granular material, over which we rolled a variety of cylinders (Figure 1). The channel was approximately 244 cm in length, 31 cm in width, and 9 cm in depth. Two granular materials were used in our experiments: PetCo aquarium sand, and Potters Industries A-100 glass beads (ballotini). Both materials had mean grain sizes near 1 mm, but the sand grains were more angular than the nearly spherical ballotini, resulting in substantially different dynamic angles of repose between the materials. The material parameters are provided in Table 1, and were taken from Sauret et al. [28], who used the same materials.

To prepare the granular bed, we filled the channel with a granular material, and then loosely scraped off the top surface layer down to a depth set using the top of the side-rails. No effort was made to compact the bed any further. To reset the bed after a disturbance to the surface, we manually stirred the material throughout its depth, and repeated the levelling procedure. On the ballotini, the cylinders typically left large (several millimetre deep) tracks as they rolled, so the surface was reset between each run. On the sand, the cylinders left tracks that were barely perceptible to the naked eye, but could be highlighted by shadows cast when the surface was illuminated from a shallow angle. The shadows revealed that the surface traversed by the cylinders had been smoothed out over the grain scale, and small levees had been left to either side of the track. To speed up the data taking process, we therefore only reset the sand surface when a large disturbance occurred (e.g. a stray cylinder). Despite the lack of any substantial surface rearrangement by the cylinders on the sand, the rolling resistance was measurably sensitive to the surface history: the resistance was noticeably different when rolling a cylinder over previous tracks (an effect familiar from the rolling of spheres over rubber and metal [6]). To reduce this affect as much as possible, we began the experiments with sand using a bedding-in procedure described in § (c).

Cylinder	M (g)	D (cm)	b (cm)	L (cm)	α	ρ_c (g/cm ³)
20	48.13	2.687	0.315	15.0	0.793	0.5658
21	72.06	3.343	0.360	15.0	0.807	0.5473
22	94.27	4.237	0.370	15.0	0.840	0.4457
23	113.56	4.857	0.385	15.0	0.854	0.4086
24	153.25	6.042	0.425	15.0	0.869	0.3563
25	246	7.288	0.560	15.0	0.858	0.3931
26	312	8.896	0.560	15.0	0.882	0.3346
27	754	21.94	0.500	16.2	0.955	0.1231
28	43.45	5.103	0.160	15.0	0.939	0.1416
29	34.84	5.094	0.145	15.0	0.944	0.1139
30	204	11.412	0.330	15.0	0.943	0.1329
31	656	11.445	0.950	15.0	0.847	0.4251
32	55.27	4.217	0.290	15.0	0.871	0.2638
36	79.50	9.559	0.155	15.0	0.968	0.0738
42	12.89	4.245	0.055	15.0	0.974	0.0607

Table 2: Reference identifier, mass M , outer diameter D , wall thickness b , length L , dimensionless moment of inertia $\alpha = I/MR^2$, and mean density ρ_c for the cylinders used in the experiments.

The cylinders were sections cut from PVC and other plastic tubing and had the radii R and masses M listed in Table 2. This table also reports the quantity $\alpha = I/MR^2$, where I is the moment of inertia, which provides a dimensionless description of the radial mass distribution, with $\alpha = 1/2$ for a uniform solid cylinder, and $\alpha \rightarrow 1$ for a thin cylindrical shell. The cylinders were sanded, cleaned, sprayed with high-visibility orange paint, and sanded again to give them consistent surface textures and appearances. A camera was mounted to the ceiling above the bed to record the cylinders' trajectories in colour at 60 frames per second with a resolution of 1920×1080 pixels. The field of view covered 2 m of the bed, providing a resolution of roughly 1 mm per pixel.

The cylinders were placed on a flat inclined ramp at the top of the runway and rolled onto the surface of the granular bed. A flexible sheet was placed over the end of the ramp to smooth the transition onto the bed and reduce any bouncing of the cylinders. The initial velocity of the cylinders as they entered the bed was controlled by adjusting the starting position of the cylinders along the ramp. Trials were discarded if they came within a few centimetres of the channel sidewalls, which tended to occur more frequently for lighter cylinders and at higher initial velocities. We repeated rolls until we recorded three to five successful trials with the same experimental parameters.

(b) Data processing

The data processing consisted of three stages. First, “image trajectories” indicating the image coordinates of the cylinders for each video frame were calculated (see Figure 1). Second, position markers on the channel were used to infer the camera's projection for the scene. Third, the “object trajectories” indicating the real-space positions of the cylinders over time were extracted by inverting the camera projection for the calculated image trajectories. For the latter, we refer to the tops of the side-rails to define a laboratory coordinate system, with X pointing along the channel, Y across it, and Z directed vertically upwards.

(i) Image trajectories

The bright orange paint of the cylinders allowed them to be precisely differentiated from the bed and the rest of the scene via colour filtering. The OpenCV 3.0 library [29] was used to

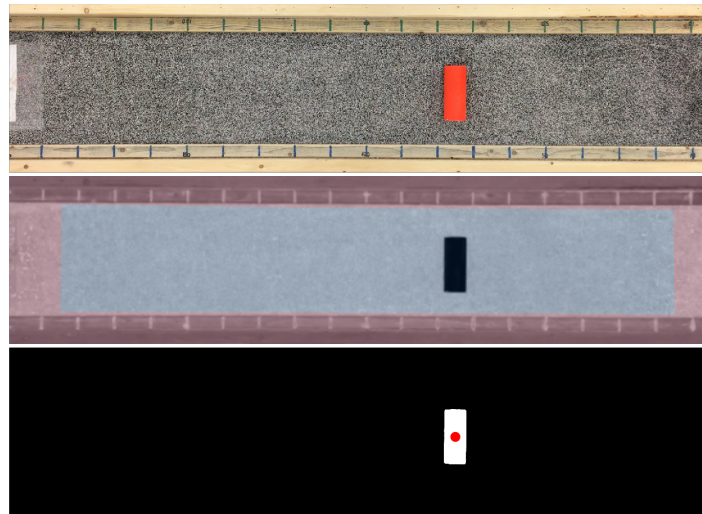


Figure 2: Stages of image-position extraction. Top: A frame from a video recording. Middle: Colour distance from reference orange, indicated in greyscale with darker pixels being closer in HSV space. The shaded red region is excluded from further processing to isolate objects on the bed. Bottom: Match field derived from the colour distance, with lighter pixels indicating a better match. The red dot indicates the centroid of the match field and defines the cylinder's image position.

extract individual frames from the videos and convert them to hue-saturation-value (HSV) colour space. We applied a light (11 pixel) Gaussian blur to each frame and computed the HSV colour distance d of each of the pixels within the granular bed from a reference orange value of (4, 205, 255). Using the colour distance d , we constructed a “match value” m for each pixel as $m = \frac{1}{2} [1 - \tanh(\frac{d-100}{5})]$, and took the centroid of match field to define the image position of the cylinder for that frame. The combination of the Gaussian blur and the smoothed match statistic dithers the edges of the cylinder, allowing for sub-pixel precision in the determination of the cylinder's image centroid. These processing stages for a sample frame are shown in Figure 2.

(ii) Camera calibration

To accurately determine the cylinder's position on the bed from its image coordinates, the camera projection was precisely characterised. We performed a standard calibration using routines from the OpenCV 3.0 library, which are based on a pinhole camera model with corrections for common modes of lens distortion. We first used images of a standard chessboard pattern to determine the camera's intrinsic projection parameters. For each scene, we then used the image positions of distance markers on the channel side rails to infer the pose of the channel relative to the camera.

The image coordinates of any point (X, Y, Z) in the laboratory frame could then be estimated by composing the best-fit pose transformation with the intrinsic camera projection. The difference between the measured image coordinates of the distance markers and the estimated image coordinates computed via this procedure constitutes the reprojection error. Our calibration procedure typically yielded reprojection errors of about 3 px.

(iii) Object trajectories

The camera and scene calibrations were used to convert the image trajectories into object trajectories describing the (X, Y) position of the cylinder centres over time for each trial. In a given image, each pixel is the projection of an entire line-of-sight in the object coordinate space. If the image coordinates and one of the object coordinates (e.g. Z) of a point is known, however,

this degeneracy can be broken and the projection inverted to determine the two remaining unknown object coordinates (e.g. (X, Y)). For each trial, we used the vertical offset of the material surface from the side rails and the radius of the cylinder to estimate the height Z of the plane containing the cylinder centre. The inversion of a cylinder's image position at this Z then yields an estimate of the (X, Y) coordinates of the centre of the cylinder over the bed. The error in this procedure is dominated by the reprojection error of the camera calibration, resulting in a systematic uncertainty of about 3 mm in the absolute positions in our object trajectories.

(c) Results

We initially tilted the channel by supported it at different heights under the two ends, and varied the angle to look for steady rolling states. We found, however, that the channel was insufficiently stiff and would flex under its own weight, resulting in a spatially-varying downslope component of gravity, as well as further errors in the calibration procedure. To avoid these issues, we laid the channel level with distributed supports to keep it flat to within 1 mm. Removing any gravitational acceleration along the bed had the further advantage of ensuring that the rolling resistance was more easily measured. However, because our results pertain to unsteady motion, they may differ from those for cylinders towed at constant speed.

In our preliminary experiments on the sand, we also explored the effect of the length of the cylinders and the depth of the granular bed on the resistance. We found that there were no significant differences in the trajectories of different length cylinders of the same PVC piping. Similarly, no significant or systematic differences were found for trials on 1, 3, 5, 7, and 9 cm deep sand beds. We therefore decided to fix the cylinder lengths to be 15 cm and the depth of the bed to be 7 cm for the sand and 2 cm for ballotini to reduce the number of parameters being varied. With these considerations, we built a dataset of over 400 trials. Plots of the trajectories for several cylinders on the ballotini are shown in Figure 3.

Two dimensional $X - Y$ plots of the trajectories are useful for identifying trials in which cylinders swerved to the side and rolled close to the side-rails, where they tended to slow down or abruptly change direction. Many trails which strayed from the centreline of the bed appeared to continue turning as they rolled (Figure 3(a)), suggesting that there may be an instability associated with perturbations away from straight or level rolling. The veering rate correlated with mean cylinder density: overall, 15% of the trials veered more than 4 cm from the centreline, but 25% of the lighter cylinders and under 10% of the heavier cylinders rolled off centre. To minimize any effects of the sidewalls on the bed dynamics, we deleted the trials that veered more than 4 cm off-centre, and used the X components of the remaining trajectories to study the kinematics of the cylinders.

The millimetre-scale accuracy of the position determination allows us to use finite differences in time to estimate the downslope velocities. Further differentiation to determine the acceleration, however, is precluded by the noise in the position measurements. In Figure 3, the cylinder accelerations are instead estimated by differentiating linear least squares fits of quadratic polynomials to the velocity data in panel (c). In general, however, we find that the form of such fits often severely biases the shape of the resulting acceleration-velocity curves (panel (d)), and ultimately, we favour the forward-modelling approach of § 4 for determining the dependence of acceleration on velocity.

For trials on the sand, where the surface was not reset between each run, we observed a systematic change in the stopping distances of the cylinders when they were first rolled over a fresh surface. We attributed this to a superficial compaction and smoothing of the top layers of grains, which affected the rolling resistance. To eliminate this effect and begin with a surface that accommodated any sideways migration of our cylinders, we therefore followed a bedding-in procedure at the beginning of the experiments: we first rolled a much longer (25 cm) cylinder down the track repeatedly until it achieved a consistent stopping distance. Despite this preliminary preparation of the surface, there were still noticeable changes in the rolling resistance when cylinders were switched. The stopping distances of the first few trials with each cylinder

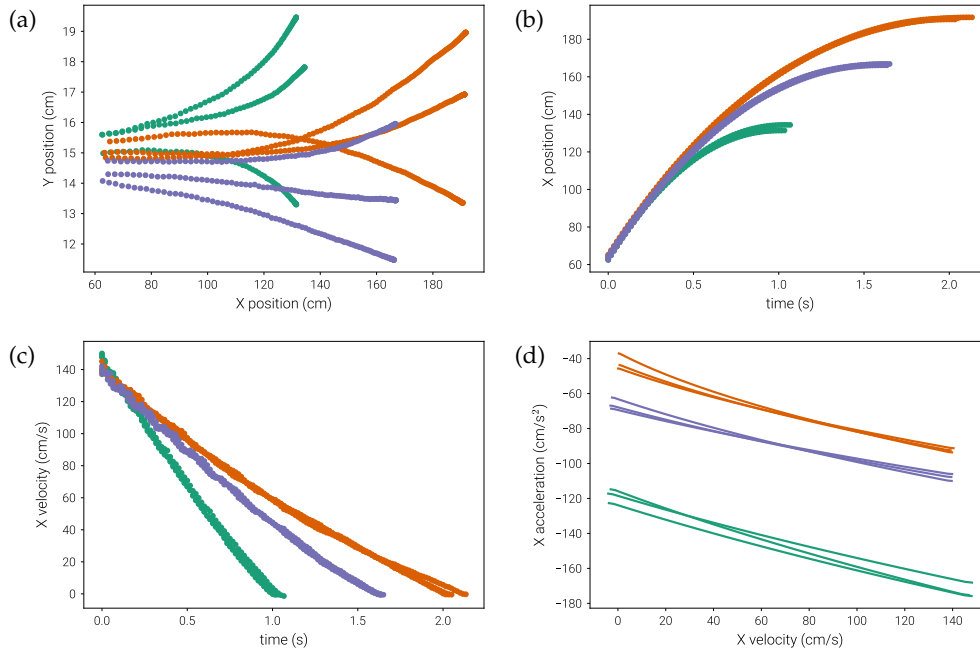


Figure 3: All trajectories for cylinder 24 (green), 29 (blue), and 36 (orange) on ballotini. (a) Two-dimensional trajectories across the bed, with a stretched aspect ratio to emphasise lateral motion. (b) Along-channel positions over time. (c) Along-channel velocities over time. (d) Along-channel accelerations versus velocity, from least-squares quadratic fits to the velocity data.

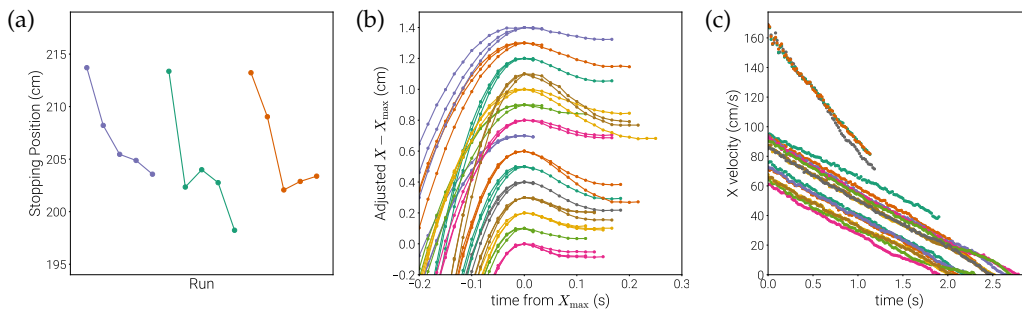


Figure 4: (a) Stopping distance of successive trials on sand for cylinders 23, 24 and 25. (b) Rollback on ballotini, showing along-channel positions against time, aligned by the time at the maximum position and vertically offset by cylinder for clarity. (c) Along-channel velocities over time of cylinder 23 on sand.

typically increased or decreased, depending on the cylinder, until saturating about 10 cm from the first stopping position (Figure 4(a)). After 3 or more trials, the stopping distances were typically reproducible to within several centimetres, leading us to discard the initial trials that showed obvious an re-bedding behaviour. Evidently, each cylinder affects the granular surface slightly differently, but we did not explore this effect in any further detail.

Another interesting feature of the rolling dynamics arises at the ends of the trajectories where the cylinders come to a stop on the bed. As shown in Figure 4(b), the cylinders tend to roll backwards several millimetres before coming to a complete stop. This effect may be due to the

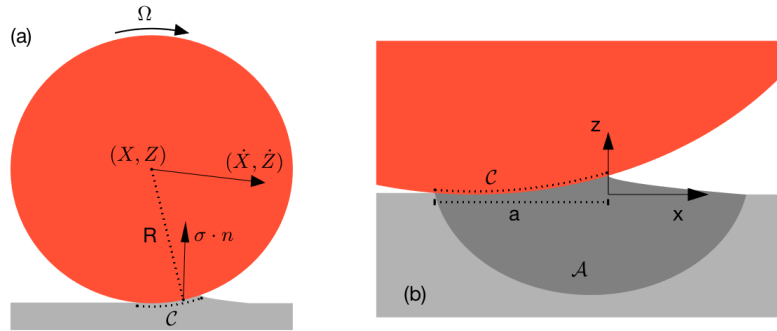


Figure 5: (a) Geometry of a rigid cylinder rolling on a deformable surface. (b) Magnification of the flowing region (dark gray, labelled \mathcal{A}) under the cylinder.

mound of grains, or “bow wave”, that builds up ahead of the cylinder and transmits the forces from the bed during rolling. Once the cylinder is arrested, however, the horizontal bed reaction becomes unbalanced, momentarily pushing the cylinder backwards.

To test the reproducibility of the dynamics, we conducted trials with a range of initial velocities for each cylinder on the sand. For initial velocities in the range of 50 – 100 cm/s, the deceleration of the cylinders did not show a pronounced dependence on the initial velocity, as can be seen in Figure 4(c). Trials with higher initial velocities around 175 cm/s, however, showed substantially larger decelerations. It was difficult to produce consistent trials at these speeds, as the cylinders would frequently bounce after leaving the ramp and veer abruptly into the side rails. We therefore exclude these higher-velocity runs from the bulk of our analysis, but note that the discrepancies in Figure 4(c) suggest that efforts to characterise rolling resistance only in terms of rolling speed may well conceal the full nature of the dynamics at high speeds.

Besides the resistance encountered due to the deformation of the granular surface, air resistance may play an important role in some trials. Taking 50 cm/s as a characteristic velocity, 6 cm as a characteristic cylinder diameter, and $\nu \approx 1.5 \times 10^{-5} \text{ m}^2/\text{s}$ for the kinematic viscosity of air, we estimate the Reynolds number of the airflow around the rolling cylinders to be of order 2000. Thus, air drag on the cylinders is expected to depend quadratically on velocity with an order-one drag coefficient. To directly measure the effect of air drag, we performed additional trials in which we rolled the cylinders over a glass sheet placed on the channel (see § 4).

Finally, several trials were examined to determine whether any sliding occurred as the cylinders rolled over the granular surface. A thin black line segment was marked on the outside of each cylinder, and the times when these lines crossed the top of the cylinders were determined from the videos. The corresponding object positions were then used to measure the distance travelled during one complete rotation. In the cases examined, this distance was indistinguishable from the cylinder circumference to within the experimental precision of $\sim 1\%$, based on our ability to determine the time at which each rotation was completed. Thus, we did not observe any noticeable slip (true or effective; see §4(b,iv)) for any trials.

3. Modelling

(a) Cylinder dynamics

To model the dynamics of the system, we consider the motion of a two-dimensional rigid cylinder rolling over a deformable granular surface. The geometry is sketched in Figure 5. We define a new cartesian coordinate system centred under the leading contact point at the neutral surface of the sand, with x pointing forward and z upward. The cylinder has radius R , mass per unit length M , and moment of inertia per unit length $I = \alpha MR^2$. The cylinder has velocity $(\dot{X}(t), \dot{Z}(t))$ and

clockwise rotation rate $\Omega(t)$. The translational and rotational dynamics of the cylinder are given by:

$$M\ddot{X} = F_x \quad (3.1)$$

$$M\ddot{Z} = F_z - Mg \quad (3.2)$$

$$I\dot{\Omega} = -T \quad (3.3)$$

where g is gravity, and (F_x, F_z) and T are the contact force and anti-clockwise torque from the underlying medium, again per unit length of the cylinder.

The contact forces are computed by integrating the surface stresses over the contact arc \mathcal{C} as

$$\begin{pmatrix} F_x \\ F_z \end{pmatrix} = \int_{\mathcal{C}} \boldsymbol{\sigma} \cdot \mathbf{n} \, d\ell, \quad (3.4)$$

where $\boldsymbol{\sigma}$ is the granular stress tensor, and \mathbf{n} and ℓ denote the cylinder normal and arc length along \mathcal{C} . The torque around the cylinder centre is given by

$$T = \int_{\mathcal{C}} (-R\hat{\mathbf{e}}_z + \mathbf{r}) \times \boldsymbol{\sigma} \cdot \mathbf{n} \, d\ell = RF_x + \int_{\mathcal{C}} \mathbf{r} \times \boldsymbol{\sigma} \cdot \mathbf{n} \, d\ell, \quad (3.5)$$

where \mathbf{r} is the position vector from the bottom of the cylinder.

The horizontal and angular momentum equations can be combined to give

$$M(\ddot{X} + \alpha R\dot{\Omega}) = F_x - \frac{T}{R} = -\frac{1}{R} \int_{\mathcal{C}} \mathbf{r} \times \boldsymbol{\sigma} \cdot \mathbf{n} \, d\ell. \quad (3.6)$$

If rolling occurs without significant slip we have $R\Omega \approx \dot{X}$, as observed to within experimental precision in our trials, and the left side of (3.6) becomes $(1 + \alpha)M\ddot{X}$. Thus, the horizontal dynamics are directly controlled by the rolling resistance,

$$F_r = \frac{1}{R} \int_{\mathcal{C}} \mathbf{r} \times \boldsymbol{\sigma} \cdot \mathbf{n} \, d\ell. \quad (3.7)$$

Below, we evaluate the integrals in (3.4) and (3.7) to leading order in the small parameter a/R , where a is the horizontal length of the contact arc, treating the sand as a plastic material satisfying the Mohr-Coulomb constitutive law. Before accomplishing this feat, we note that if the surface stresses are $O(\rho_s g a)$, then F_x and F_z are formally $O(\rho_s g a^2)$ from (3.4), while F_r is $O(\rho_s g a^3/R)$ from (3.7). However, if $R\Omega \approx \dot{X}$ (3.1) and (3.6) imply $(1 + \alpha)F_x = -F_r$, so $F_x \sim F_r$. This can only be arranged if F_x turns out to contain a small numerical factor of order a/R , in which case $F_x \sim (a/R)F_z$. For the contact area to remain small during rolling, \dot{Z} and \ddot{Z} must also be $O(a/R)$ in comparison to \dot{X} and \ddot{X} . With these scalings and (3.1), we then have that $M\ddot{Z} \sim M\dot{X}(a/R) \sim F_x(a/R) \sim F_z(a/R)^2$. The roller is therefore in vertical equilibrium to leading order, with $F_z \approx Mg$ in (3.2). This allows us to estimate the magnitude of the horizontal accelerations as $\ddot{X} = F_x/M \sim (F_z/M)(a/R) \sim g(a/R) \ll g$, in line with the experimental results (see Figure 3). We also have that $F_z \approx Mg \sim \rho_s g a^2$ and $M \sim \rho_c R^2$, and so the contact area scales as $(a/R) \sim \sqrt{\rho_c/\rho_s}$, which is 0.2 – 0.6 for the experimental cylinders.

(b) Sand dynamics

(i) Slipline theory

To form a tractable model, we neglect inertial forces in the bed, which scale like $\dot{X}\Omega$ and should be small relative to gravity for the larger cylinders and low-velocity portions of the trials. The

quasi-static equations of force balance for the granular stresses are then

$$\frac{\partial \sigma_{xx}}{\partial x} + \frac{\partial \sigma_{xz}}{\partial z} = 0 \quad \& \quad \frac{\partial \sigma_{xz}}{\partial x} + \frac{\partial \sigma_{zz}}{\partial z} = \rho_s g, \quad (3.8)$$

For the stresses, we use the Mohr-Coulomb plastic constitutive law [24], which we write in the form,

$$\begin{aligned} \sigma_{xx} &= -p + p \sin \phi \cos 2\theta \\ \sigma_{zz} &= -p - p \sin \phi \cos 2\theta \\ \sigma_{xz} &= p \sin \phi \sin 2\theta, \end{aligned} \quad (3.9)$$

where ϕ is the internal angle of friction, p is the mean compressive stress, and θ is the anti-clockwise angle from the horizontal to the direction of the least compressive stress. With this rheology the stress field is conveniently represented in terms of its characteristic curves, the sliplines. These curves are composed of two families; the α -lines are defined by

$$dz = \tan(\theta - \varepsilon) dx, \quad dp + 2p \tan \phi d\theta = -\rho_s g(dz + \tan \phi dx), \quad (3.10)$$

whereas the β -lines satisfy

$$dz = \tan(\theta + \varepsilon) dx, \quad dp - 2p \tan \phi d\theta = -\rho_s g(dz - \tan \phi dx), \quad (3.11)$$

with

$$\varepsilon = \frac{\pi}{4} + \frac{\phi}{2}. \quad (3.12)$$

(ii) Boundary conditions

We calculate the leading-order forces in the small parameter a/R , for which it is sufficient to linearise the surface conditions about $z = 0$. In the coordinate system centred at the leading edge, the section $-a < x < 0$ is the contact surface \mathcal{C} , and the section $x > 0$ is a free surface.

We impose a friction condition beneath the cylinder that translates to demanding that

$$\theta = \theta_f \quad \text{on } z = 0, \quad -a < x < 0. \quad (3.13)$$

If the surface is perfectly smooth, $\theta_f = 0$ so that $\sigma_{xz} = 0$ and $\sigma_{zz} = -p(1 + \sin \phi)$. If it is perfectly rough, $\theta_f = -\varepsilon$ and the β -lines are parallel to the surface. If δ denotes the surface friction angle, then $\theta_f = \frac{1}{2}\delta + \frac{1}{2}\sin^{-1}(\sin \delta / \sin \phi)$.

The free surface ahead of the contact area is in a state of compression with

$$p = 0, \quad \theta = \frac{1}{2}\pi, \quad \text{on } z = 0, \quad x > 0 \quad (3.14)$$

so that $\sigma_{xz} = \sigma_{zz} = 0$. This leads to a subsurface triangular region (a “Rankine zone”) where the stress is hydrostatic ($\sigma_{zz} = \rho_s g z$ and $p = -\rho_s g z / (1 - \sin \phi)$), and the characteristics are straight lines inclined at angles $\pm \varepsilon$ to the vertical.

(iii) Separable solution

The problem permits a self-similar solution corresponding to a separable form in polar coordinates (r, ψ) [24]. We set

$$x = r \cos \psi \equiv \Xi \xi(\psi), \quad z = r \sin \psi \equiv \Xi \zeta(\psi), \quad p = \rho_s g r \Sigma(\psi), \quad \theta = \Theta(\psi), \quad (3.15)$$

where Ξ is an undetermined lengthscale. The stress equations then reduce to

$$\Sigma' = \frac{\Sigma \sin(2\Theta - 2\psi) - \cos(2\Theta - \psi)}{\sin \phi + \cos(2\Theta - 2\psi)} \quad (3.16)$$

$$\Theta' = \frac{\sin \psi + \sin \phi \sin(2\Theta - \psi) + \Sigma \cos^2 \phi}{2\Sigma \sin \phi [\sin \phi + \cos(2\Theta - 2\psi)]}. \quad (3.17)$$

There are singular points in the system (3.16)-(3.17) where $\sin \phi + \cos(2\Theta - 2\psi) = 0$. One such point always occurs at the border with the triangular Rankine zone ahead of the self-similar region

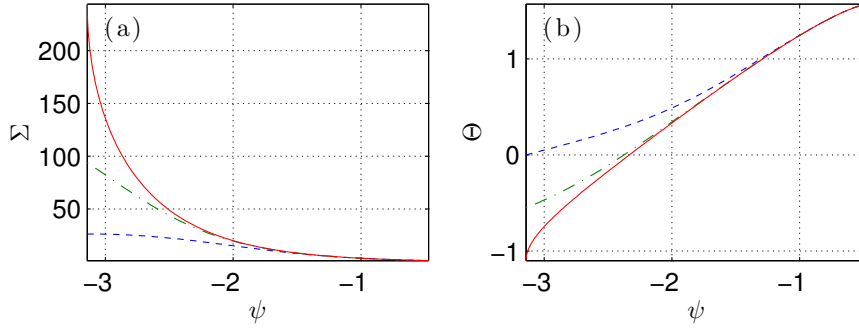


Figure 6: Self-similar solutions for (a) $\Sigma(\psi)$ and (b) $\Theta(\psi)$ with $\phi = 36^\circ$ for smooth ($\theta_f = 0$; dashed), semi-rough ($\theta_f = -\frac{1}{2}\varepsilon$; dot-dashed), and rough ($\theta_f = -\varepsilon$; solid) cylinders.

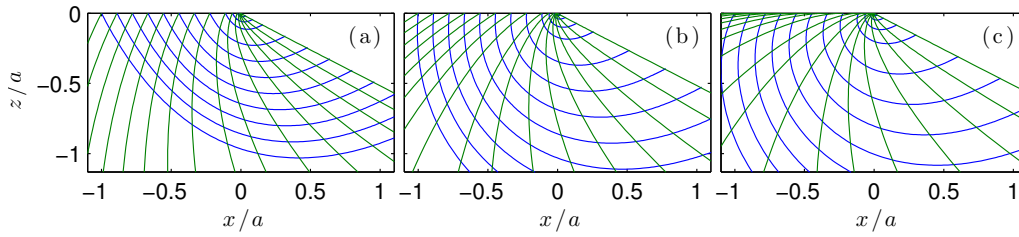


Figure 7: Self-similar slipline fields with $\phi = 36^\circ$ for (a) smooth ($\theta_f = 0$), (b) semi-rough ($\theta_f = -\frac{1}{2}\varepsilon$), and (c) rough ($\theta_f = -\varepsilon$) cylinders.

where we must impose the boundary condition

$$\Theta(\varepsilon - \frac{1}{2}\pi) = \frac{1}{2}\pi, \quad (3.18)$$

to match to the Rankine zone. Here, we further demand that the solution be regular, which automatically sets the pressure to its hydrostatic value, fixing $\Sigma(\varepsilon - \frac{1}{2}\pi) = -\sin \psi / (1 - \sin \phi)$ without explicitly adding this as a second boundary condition.

For $\psi \rightarrow -\pi$, we impose $\Theta(-\pi) = \theta_f$. For the perfectly rough case when $\theta_f = -\varepsilon$, this second boundary is also a singular point. Moreover, we cannot impose regularity in view of the imposition of all the boundary conditions already. Instead, the derivative of the solution diverges and we exploit the local solution,

$$\Theta + \varepsilon \sim \sqrt{\frac{|\psi + \pi| [1 + \Sigma(-\pi) \cot \phi]}{2\Sigma(-\pi)}}, \quad (3.19)$$

to impose the boundary condition at an angle slightly below $-\pi$. Numerical solutions for rough, semi-rough and smooth cylinders are shown in Figure 6.

Given $\xi(\psi) = \zeta(\psi) \cot \psi$ along each characteristic, we have

$$\zeta' = \frac{\zeta \sec^2 \psi \cot \psi}{1 - \tan \psi \cot(\Theta \mp \varepsilon)}. \quad (3.20)$$

We may solve this ODE subject to $\zeta \rightarrow 0$ for $\psi \rightarrow -\pi$, implying $\xi \rightarrow -1$. The resulting curves $(x, z) = \Xi(\xi_{\alpha, \beta}(\psi), \zeta_{\alpha, \beta}(\psi))$, corresponding to the two choices of sign in (3.20), generate the slipline field through the scaling Ξ . Examples are shown in Figure 7.

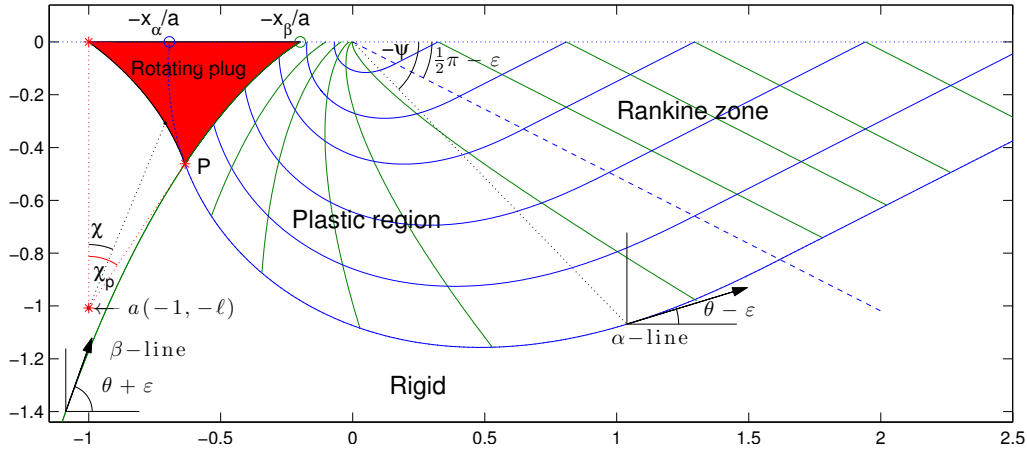


Figure 8: Sketch of the geometry for the Collins slipline solution in the limit of small deformation. The contact area occupies $-1 < x/a < 0$, and the bow wave extends in front of the cylinder over $x/a > 0$. The angle subtended by the rotating plug is $\chi_p \equiv \varepsilon - \Theta(\psi_p) - \phi$. The slipline field is plotted for $\phi = 36^\circ$, $\theta_f = -\frac{1}{2}\varepsilon$, and $\psi_p = -4\pi/5$.

(iv) Collins construct

As seen below, the surface forces acting on the cylinder that are predicted by the separable solution cannot be adjusted to ensure that $F_x = O(\rho_s g a^3/R)$ in accordance with the cylinder dynamics discussed in § 3(a). This motivates a modification of the separable solution that follows Collins' solution for a cohesive ideal plastic deforming underneath a roller [26]. We attach a plug of grains to the surface of the cylinder, such that the roller and plug rigidly rotate about a point (x_o, z_o) beneath the granular surface. For the back surface to depart tangentially from the cylinder, the rotation centre must lie along the line connecting the back contact point with the centre of the cylinder. If we define Υ to be the angle this line makes with the vertical, and $a\ell$ to be the distance from (x_o, z_o) to the back contact point, then we have

$$(\dot{X}, \dot{Z}) = (R + a\ell)\Omega(\cos \Upsilon, -\sin \Upsilon). \quad (3.21)$$

With $a \ll R$ and $\dot{Z} = O(a\dot{X}/R)$, we must have that $\Upsilon = O(a/R)$, $(x_o, z_o) \sim -a(1, \ell)$, and

$$\dot{X} = R\Omega + a\ell\Omega + O(a^2\Omega/R), \quad (3.22)$$

as illustrated in Figure 8. Thus, there is an effective slip with speed $\dot{X} - R\Omega \approx a\ell\Omega$, even though there is no true slip between the surfaces.

Ahead of the plug, the material deforms plastically and the separable solution applies. Because the border between the rotating plug and this plastic region is a yield surface, it must also follow a slip-line; we choose this to be a specific one of the self-similar β -lines intersecting the contact surface at $(-x_\beta, 0)$ (see Figure 8). This β -line continues down to the point P where it intersects the lowest α -line, which bounds the entire yielded region. The left-hand border of the rotating plug divides that region from the immobile grains below, and for a Mohr-Coulomb material following an associated flow rule, must form a logarithmic spiral maintaining a pitch angle ϕ with the circular velocity of the plug material [30]. The shape of the log-spiral is given by

$$x_s(\chi) = -a + ae^{-\chi \tan \phi} \sin \chi \quad \& \quad z_s(\chi) = -a\ell + ae^{-\chi \tan \phi} \cos \chi, \quad (3.23)$$

where χ is the angular position relative to (x_o, z_o) , measured clockwise from the vertical. This log-spiral continues the lowest α -line to the origin, and meets that characteristic tangentially at

the point P . This geometry demands that

$$\ell = \frac{-\sin \psi_p}{e^{-\chi_p \tan \phi} \cos[\psi_p + \chi_p] - \cos \psi_p}, \quad (3.24)$$

where ψ_p is the polar angle of the intersection point and $\chi_p = \varepsilon - \Theta(\psi_p) - \phi$. The lowest α -line is given by $(x, z) = x_\alpha(\xi_\alpha, \zeta_\alpha)$, and the β -line bordering the rotating plug is $(x, z) = x_\beta(\xi_\beta, \zeta_\beta)$, where

$$x_{\alpha,\beta} = \frac{z_s(\chi_p)}{\zeta_{\alpha,\beta}(\psi_p)}. \quad (3.25)$$

The stress along the failure surface underlying the rotating plug is not given by the separable solution. Instead, the requirement that the log-spiral continues the lowest α -line, in conjunction with the yield criterion, implies that

$$\frac{dp}{d\chi} = 2p \tan \phi + \rho_s g a \ell \sec^2 \phi e^{-\chi \tan \phi} \sin \chi. \quad (3.26)$$

and $\theta = \varepsilon - \chi - \phi$. Equation (3.26) can be integrated from $\chi = \chi_p$ up to $\chi = 0$, assuming that the pressure is continuous and matches with that of the separable solution at P (no boundary condition is therefore applied at the back contact point, in line with previous constructions [21,22]).

(v) Forces and torques

We let \mathcal{L} denote the contour combining the log-spiral and β -line that border the plug with the section of the contact surface from $(-x_\beta, 0)$ to the origin. The forces acting on this contour are the same as the forces acting on the cylinder modulo the contributions from the weight of the rotating plug. We therefore write the forces in (3.4) and (3.7) as

$$F_x = \hat{F}_x, \quad F_z = \hat{F}_z - \iint_A \rho_s g \, dA, \quad F_r = \hat{F}_r - \iint_A (a + x) \rho_s g \, dA, \quad (3.27)$$

where the integrals are taken over the area A of the plug, and where \hat{F}_x , \hat{F}_z and \hat{F}_r are the forces acting on \mathcal{L} . These are given by

$$\begin{pmatrix} \hat{F}_x \\ \hat{F}_z \end{pmatrix} = \int_{\mathcal{L}} p \begin{pmatrix} 1 - \sin \phi \cos 2\theta & -\sin \phi \sin 2\theta \\ -\sin \phi \sin 2\theta & 1 + \sin \phi \cos 2\theta \end{pmatrix} \cdot \mathbf{n} \, ds, \quad (3.28)$$

and

$$\hat{F}_r = \frac{1}{R} \int_{\mathcal{L}} \mathbf{r} \times p \begin{pmatrix} 1 - \sin \phi \cos 2\theta & -\sin \phi \sin 2\theta \\ -\sin \phi \sin 2\theta & 1 + \sin \phi \cos 2\theta \end{pmatrix} \cdot \mathbf{n} \, ds \quad (3.29)$$

where \mathbf{n} denotes the outward normal to \mathcal{L} . These integrals can be calculated using the separable solution and (3.26) for p and θ . Since the pressure scales with the weight of the material, $\rho_s g a$, the contact length a can be scaled out and the resulting forces written in terms of dimensionless functions as

$$F_x = \rho_s g a^2 \mathcal{F}_x(\ell; \phi, \theta_f) \quad F_z = \rho_s g a^2 \mathcal{F}_z(\ell; \phi, \theta_f) \quad F_r = \frac{a}{R} \rho_s g a^2 \mathcal{F}_r(\ell; \phi, \theta_f). \quad (3.30)$$

Sample solutions for the force functions $\mathcal{F}_x(\ell; \phi, \theta_f)$, $\mathcal{F}_z(\ell; \phi, \theta_f)$ and $\mathcal{F}_r(\ell; \phi, \theta_f)$ are shown in Figure 9(a) for a perfectly rough cylinder with $\phi = 36^\circ$. The horizontal and vertical stresses along \mathcal{L} for a specific choice of ℓ (corresponding to the solution in Figure 8) are shown in Figure 10. The stresses for the separable solution grow linearly with position along the line of contact as indicated by the plots for $x > -x_\beta$ in (b); the redistribution of stress along the contour \mathcal{L} due to the presence of the rotating plug modifies the total bed reaction, reducing $\mathcal{F}_x(\ell)$ and generating stress jumps at the switches between the different pieces of \mathcal{L} .

As argued earlier, the angular and horizontal accelerations can only be consistent with one another provided that F_x is small. In particular, we must have $\mathcal{F}_x = O(a/R)$, which demands that ℓ must be close to the value $\ell = \ell_*$ that gives $\mathcal{F}_x(\ell_*; \phi, \theta_f) = 0$. Note that the result for the

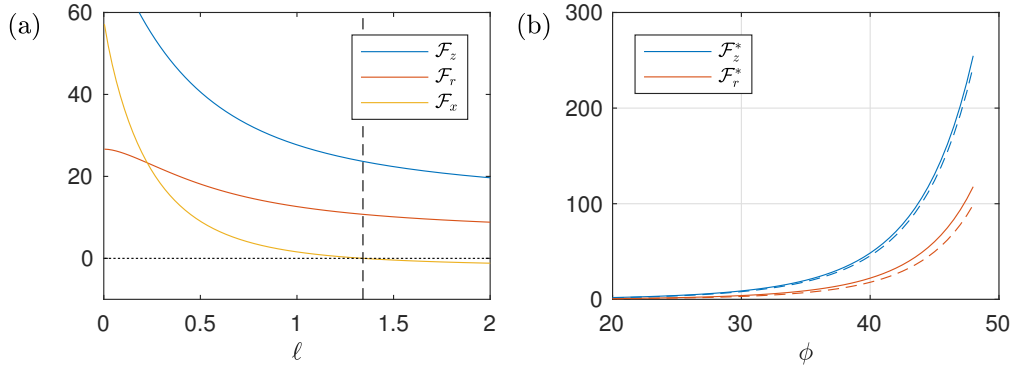


Figure 9: (a) Dimensionless force functions for the Collins solution, for $\phi = 36^\circ$ and a perfectly rough cylinder. The vertical dashed line indicates the location $\ell = \ell_*$ at which $\mathcal{F}_x = 0$. (b) Lift force $\mathcal{F}_z^* = \mathcal{F}_z(\ell_*; \phi, \theta_f)$ and rolling resistance $\mathcal{F}_r^* = \mathcal{F}_r(\ell_*; \phi, \theta_f)$ as a function of internal frictional angle. Solid lines show the perfectly rough case; dashed lines show the result for $\theta_f = -\varepsilon/10$.

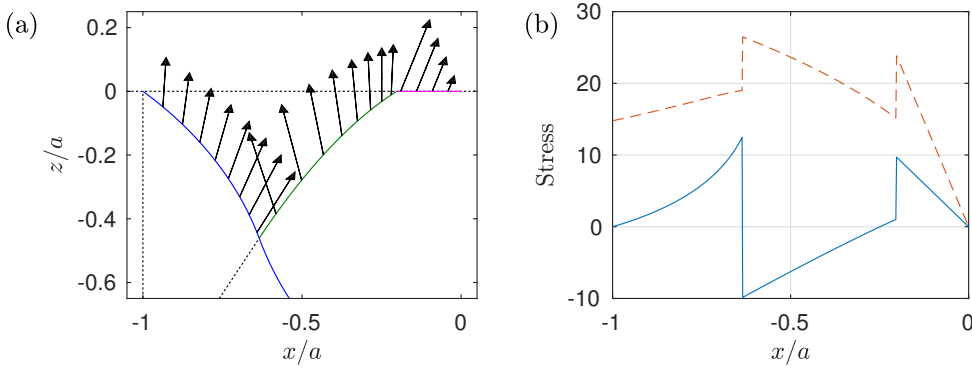


Figure 10: Dimensionless horizontal and vertical stresses on the contour \mathcal{L} for the solution shown in Figure 8; (a) shows stress vectors (force per unit length), whereas (b) plots the horizontal (solid) and vertical (dashed) stress components.

separable solution (with no attached plug) is recovered by taking $\ell = 0$, which indicates that this case cannot furnish consistent horizontal and angular accelerations on the cylinder.

To leading order we therefore find

$$F_z \sim \rho_s g a^2 \mathcal{F}_z^* \quad \text{and} \quad F_r \sim \frac{a}{R} \rho_s g a^2 \mathcal{F}_r^*, \quad (3.31)$$

where $[\mathcal{F}_z^*, \mathcal{F}_r^*] \equiv [\mathcal{F}_z(\ell_*; \phi, \theta_f), \mathcal{F}_r(\ell_*; \phi, \theta_f)]$. The two special values \mathcal{F}_z^* and \mathcal{F}_r^* are plotted as functions of ϕ in Figure 9(b) for a perfectly rough and a semi-rough cylinder. Even though the semi-rough case is almost smooth ($\theta_f = -\varepsilon/10$), the change in the dimensionless force function is very slight. Thus, the rolling resistance is expected to be insensitive to the roughness of the surface of the cylinder. One could also envision a situation in which the cylinder slides over the granular bed (and the rotating plug) in the manner of true slip when the net normal force over the contact line is small in comparison to the total tangential force. This situation is ruled out for surface friction coefficients of order unity when $\ell \sim \ell_*$, as this guarantees that the tangential force on the surface is $O(a/R)$ relative to the normal force.

In Appendix A, we proceed further with the model and also compute the velocity field of the deforming granular bed, which allows one to determine the shape of the free surface in the bow wave ahead of the roller. Two significant problems emerge with this construction when using the traditional Mohr-Coulomb model: the leading-order velocity field diverges at the front contact point and the free surface descends unphysically below the bottom of the rolling cylinder. Both problems are absent for a cohesive material (Appendix B), and arise here because the standard Mohr-Coulomb model predicts an excessive degree of dilation during flow, which is a known deficiency of the theory [31,32] and can be cured by introducing a relatively small angle of dilation (see Appendix A).

4. Analysis

To compare with the predictions of the plasticity theory, we fit the experimental data to model trajectories given by a force law with constant and quadratic velocity terms:

$$\ddot{X} = C_0 + C_2 \dot{X}^2. \quad (4.1)$$

Before performing the fits, we truncated the trajectories once their velocities dropped below 5 cm/s to prevent stopping effects such as the rollback in Figure 4(b) from affecting the parameters of the fit. We then performed a nonlinear least-squares fit to the solutions of (4.1) on all trials for each cylinder and granular material combination, using the initial position and velocity for each trial and the force-law coefficients C_0 and C_2 as parameters. Uncertainties in the fitted parameters were determined using the covariances from the nonlinear fit, scaled by the square-root of the 95th percentile of the corresponding χ^2 distribution, with the uncertainties in the position data all taken to be 3 mm.

The fitting results for trials on the glass sheet, sand, and ballotini are shown in Figure 11. The fits for the glass sheet show a small constant resistance and a more substantial quadratic component, suggesting that air drag provides the dominant resistance in these trials. In this case, C_2 is related to the cylinder's drag coefficient C_d by

$$C_2 = -\frac{1}{2\pi} \frac{\rho_a}{\rho_c} \frac{C_d}{R(1+\alpha)}. \quad (4.2)$$

The average of the fitted C_2 values suggests that $C_d = 2.7 \pm 0.3$ for cylinders rolling on a flat surface.

For most cylinders on both the ballotini and sand, the fitted values of C_0 and C_2 indicate that the velocity-dependent component of the acceleration is less significant than the constant drag at the typical velocities of our trials. The ballotini shows a substantially larger constant resistance than the sand, but the two typically show comparable quadratic components. In both cases, the fitted C_2 values are roughly an order of magnitude larger than those expected from air resistance, indicating that there is some velocity-dependent rolling resistance for these materials.

If the cylinder is in vertical equilibrium ($F_z = Mg$) and is fully rough, the leading-order vertical force predicted by the model can be used to solve for the contact length a as

$$\left(\frac{a}{R}\right)^2 = \frac{\rho_c}{\rho_s} \frac{\pi}{\mathcal{F}_z^*}, \quad (4.3)$$

with the internal friction angle of each bed material determined from its dynamic angle of repose via $\sin(\phi) = \tan(\phi_c)$ [18]. This estimate improves the prediction from dimensional analysis given earlier and suggests that $a/R \approx 0.1$ and 0.4 for our experiments with sand and ballotini, respectively. The leading-order prediction for the rolling resistance can now be written as the constant acceleration,

$$C_{0,\text{theory}} = -\frac{g}{1+\alpha} \left(\frac{a}{R}\right) \frac{\mathcal{F}_r^*}{\mathcal{F}_z^*} = -\frac{g}{1+\alpha} \left(\frac{\rho_c}{\rho_s}\right)^{1/2} \Gamma(\phi, \theta_f), \quad \Gamma(\phi, \theta_f) = \sqrt{\frac{\pi \mathcal{F}_r^{*2}}{\mathcal{F}_z^{*3}}}. \quad (4.4)$$

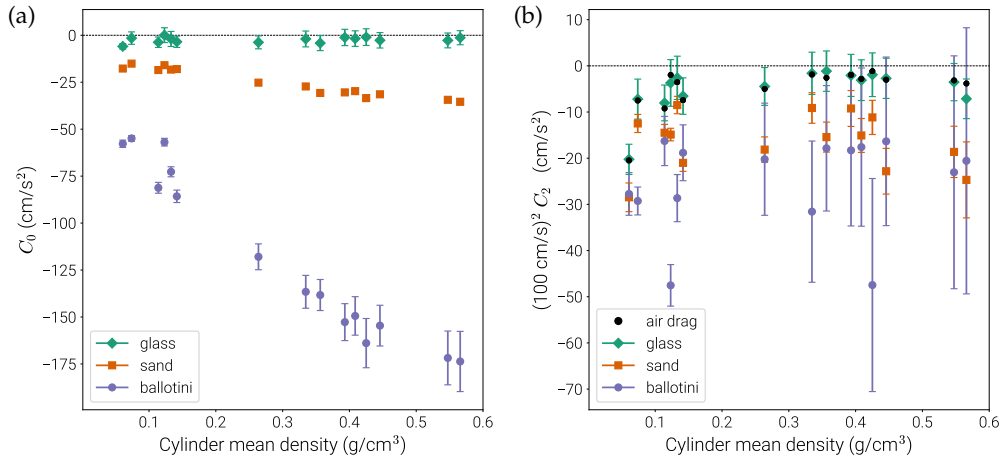


Figure 11: Best fitting force-law coefficients for cylinders rolling on the glass sheet, sand, and ballotini, showing (a) C_0 and (b) C_2 in (4.1). In (b), the points labelled “air drag” refer to the estimate (4.2) with $C_d = 2.7$.

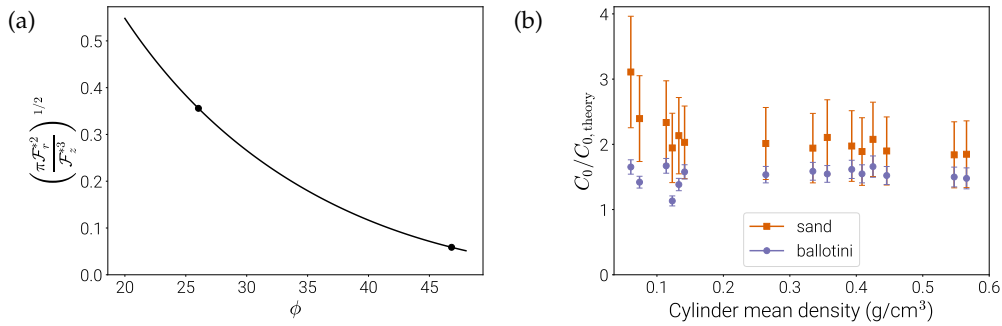


Figure 12: (a) The factor Γ in (4.4) as a function of internal friction angle, with the values for ballotini and sand indicated by dots. (b) Comparison between fitted and model rolling resistance. Both are plotted for a fully rough cylinder surface ($\theta_f = -\varepsilon$).

The dimensionless factor Γ in (4.4) is plotted as a function of internal friction angle in Figure 12(a). Somewhat counterintuitively, this factor decreases with the internal friction, because although the drag force F_r increases with ϕ , the contact area needed to support the weight of the cylinder decreases more strongly with friction. In other words, the roller digs into the medium more for lower ϕ , increasing the rolling resistance, as seen in the experiments where the cylinders encounter greater resistance when rolling over the ballotini in comparison to sand. A more detailed comparison of theory and experiment is shown in Figure 12(b), which shows the ratio between the fitted C_0 values for sand and ballotini and the model prediction in (4.4), including the uncertainty in the friction angle for each material. The theory under-predicts the fitted resistances by roughly 50% for both the sand and the ballotini, but correctly captures the overall magnitude of the rolling resistance and its scaling with the cylinder’s mean density.

Unfortunately, the trajectory fits typically show strong covariances between C_2 and the initial velocities of the faster trials, which limits our confidence in the inferred values of these parameters. Moreover, different forms for the velocity dependence of the force law (such as a

linear form) lead to trajectories that do not fit the data any more or less conclusively. We cannot therefore characterise the velocity dependence of the resistance in any further detail.

5. Conclusion

We have experimentally investigated the resistance experienced by cylinders rolling on two dry granular media, a relatively coarse sand and ballotini (glass spheres). The cylinders were relatively long and light, with low mean densities compared to the granular materials, which distinguishes our study from some earlier experiments with spheres [17] and the bulk of the literature on wheels. Thus, surface deformations are expected to be localised and superficial. This allows us to model the bed as two-dimensional and in the asymptotic limit that the deforming contact region is much smaller than the cylinder radius, and the deflection of the free surface is slight [19–21]. We further adopted the cohesionless Mohr-Coulomb law to describe the granular rheology. The resulting model predicts that the rolling resistance is independent of cylinder velocity, scaling with the square-root of the ratio of mean densities.

The trajectories of cylinders in the experiment were fitted using a simple drag law in which rolling resistance consisted of an overall constant plus a rate-dependent part that was quadratic in cylinder speed, similar to that expected for air drag. The measured drag was dominated by the constant term at the velocities typical of our experiments. However, the quadratic component was larger than that expected for air drag, which was estimated by rolling the cylinders down a flat glass surface. Thus, the rolling resistance appears to contain an effect stemming from rate-dependent granular rheology. We did not, however, attempt to include such effects into the rheology of our theoretical model, as might be feasible by exploiting recently proposed semi-empirical friction laws [18].

Nevertheless, the basic drag constant measured in the experiments is, to within a factor of two, consistent with that predicted by the Mohr-Coulomb plasticity model, and matches the predicted dependence on the ratio of mean densities. One important feature of the model is the characteristic flow pattern underneath the rolling cylinder. Following Collins [26], we have represented this pattern in terms of a region of plastic deformation below the front contact point which extends up to the free surface ahead of the cylinder, and back to a plug that is rigidly attached to the roller. The plug rigidly rotates with the cylinder and slides along a log-spiral failure surface over the static grains underneath. The rotating plug incorporates a finite, but small, effective slip of the cylinder as it rolls due to granular deformation, as in Reynolds' [5] original image of the mechanism underlying rolling friction. Crucially, the plug also reorients the forces that are exerted by the bed such that the net horizontal force on the cylinder can be made small in accordance with its equations of motion. Without this reorientation, there is a physical inconsistency between the angular and horizontal momentum equations that precludes a rolling state.

Several extensions to the experiments may allow a better determination of rolling resistance of light cylinders on granular media: a longer bed would permit one to record trajectories with a larger range of velocities, and further improvement to the scene calibration would allow better inference of the cylinder trajectories in physical space, both of which would help to constrain the velocity dependence of the drag. An experimental setup with a more precise launching mechanism and a faster way to resurface the bed would help eliminate unsuccessful trials and reduce their lateral motion and history dependence. However, such effects are interesting in their own right, and may be important to any practical applications of rolling over granular media. In particular, the sideways veering of the cylinders as they leave the centreline of the channel is suggestive of an instability that deserves further exploration.

Data Accessibility. The trial metadata and object trajectories are available online at http://data.keaton-burns.com/rolling_data/.

Authors' Contributions. KB performed the experiments, performed the data processing and analysis, assisted with the modelling, and helped draft the manuscript. NB supervised the experiments, assisted with

the modelling, and drafted the manuscript. IH assisted with the experiments, performed the modelling, and helped draft the manuscript.

Acknowledgements. We thank Anders Jensen for assistance constructing the experimental apparatus. We thank Jim Hambleton for critical comments and pointing out an error in the first draft of this paper.

Funding. Experiments and modelling were conducted at the 2016 Geophysical Fluid Dynamics Summer Study Program, Woods Hole Oceanographic Institution, which is supported by the US National Science Foundation and US Office of Naval Research.

Competing Interests. We have no competing interests.

A. Velocity field and free surface shape

In a generalisation of Mohr-Coulomb theory, the characteristic curves of the velocity field (u, w) are given by

$$dz = \tan(\theta - \frac{1}{4}\pi - \frac{1}{2}\nu)dx, \quad du + \tan(\theta - \frac{1}{4}\pi - \frac{1}{2}\nu)dw = 0, \quad (\text{A } 1)$$

and

$$dz = \tan(\theta + \frac{1}{4}\pi + \frac{1}{2}\nu)dx, \quad du + \tan(\theta + \frac{1}{4}\pi + \frac{1}{2}\nu)dw = 0, \quad (\text{A } 2)$$

where ν is the angle of dilation such that

$$u_x + w_z = \sin \nu \sqrt{(u_x - w_z)^2 + (u_z + w_x)^2}. \quad (\text{A } 3)$$

(e.g. [31,32]). Only when $\nu = \phi$, as in the traditional Mohr-Coulomb model, do the characteristics of the stress and velocity fields coincide.

To construct the velocity fields associated with our leading-order stress field solutions, we integrate (A 1) and (A 2) numerically using centred differences on a grid defined by the characteristics of the velocity field, exploiting the self-similar solution for θ . We begin the integration along the lowest α -line within the yielded region and the β -line forming the yielded edge of the rotating plug. If these stress characteristics are not also velocity characteristics ($\nu \neq \phi$), the velocity must be prescribed on both of these borders to match with the stationary unyielded material below and the rigidly rotating plug to the back. If $\nu = \phi$, the borders are velocity characteristics and slip is allowed along them, provided it occurs at angle ϕ to the characteristics. The numerical integration then progresses upward and rightward to furnish the velocity field over the characteristic web underneath the last velocity characteristic leaving the top right corner of the rotating plug. Above this curve, the characteristics no longer begin from the plug, but from the yielded section of the x -axis. There, the $z = 0$ intercepts of the upcoming characteristics must be found, and new downward characteristics launched to complete the web throughout the yielded region, taking the prescribed normal velocity $w = -\Omega(a + x)$ as the boundary condition.

The velocity field computed for the parameter values of Figure 8 is shown in Figure 13 for $\nu = \phi$ and $\nu = 0$. In the first case, the velocity becomes arbitrarily large at the right-hand edge of the contact region, as for the problem of a critically loaded foundation [25], which reflects the well-known deficiency of the traditional Mohr-Coulomb model in predicting excessive dilation during flow. Neglecting inertial terms in the bed dynamics requires that the sand velocities are $\lesssim a\Omega$ (given that $\dot{X}\Omega \lesssim g$ for the experiments), which is not satisfied by this model. By contrast, a dilation angle of $\nu = 0$ furnishes an incompressible flow with velocities $\lesssim a\Omega$ that is free of this singularity, but has velocity characteristics that no longer coincide with those of the stress, and which exposes a stationary, yielded zone underneath the flow region. Note that, to remain consistent with incompressibility, the rigidly rotating plug is now bordered from below by a circular arc which joins smoothly onto a velocity characteristic in the yielded region, and along which the stress is not prescribed by (3.26). Thus, the predictions for the rolling resistance no longer apply when $\nu \neq \phi$.

Let $z = h = O(a^2/R)$ denote the position of the granular surface. For nearly steady rolling ($\dot{Z} \approx 0$), the back contact point lies at the bottom of the roller and the kinematic condition for

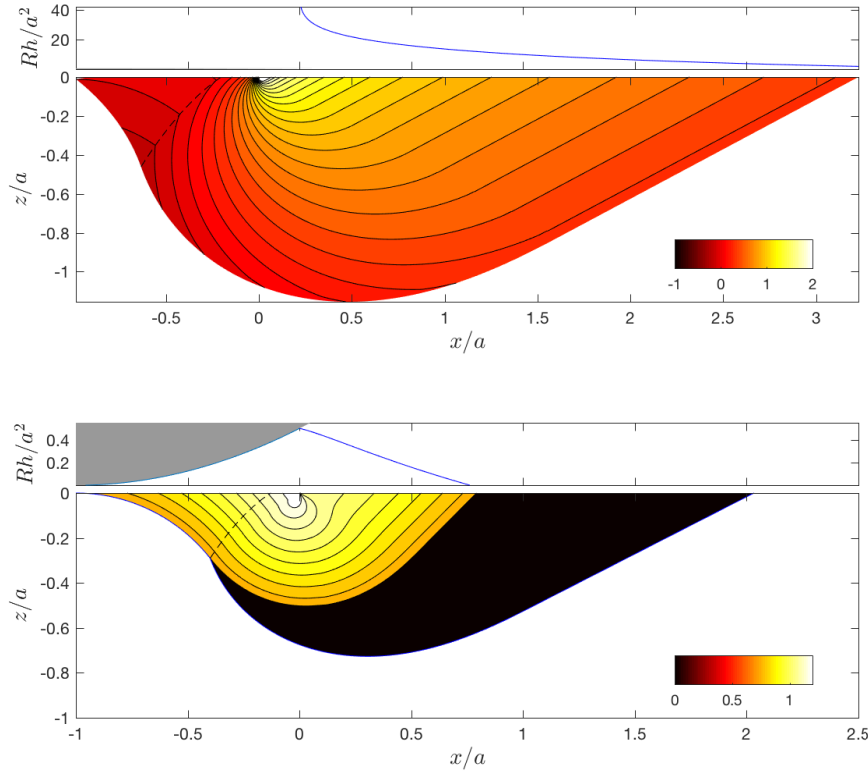


Figure 13: Speed contours for $\phi = 36^\circ$, $\psi_p = -4\pi/5$, $\theta_f = -\frac{1}{2}\varepsilon$. Top: $\log_{10}(\sqrt{u^2 + w^2}/a\Omega)$ for $\nu = \phi$. Bottom: $\sqrt{u^2 + w^2}/a\Omega$ for $\nu = 0$. For each, the predicted free surface shape is shown above.

the free surface becomes $-\dot{X}h_x = w + O(a^2\dot{X}/R^2)$. Hence,

$$h = \int_x^{x_f} \frac{w}{\dot{X}} dx = h_b + \frac{a^2}{2R} - \int_0^x \frac{w}{\dot{X}} dx \quad \text{for } 0 < x < x_f, \quad (\text{A } 4)$$

where $h_b = h(-a)$, x_f denotes the front of the bow wave (where $h = 0$), and we have matched to the contact arc below the roller, where $h = h_b + (x + a)^2/(2R)$ for $-a < x < 0$. Note that

$$\iint_{\mathcal{A}} (u_x + w_z) dx dz = \int_0^{x_f} w(x, 0) dx - \frac{1}{2}a^2\Omega = \dot{X}h_b, \quad (\text{A } 5)$$

where \mathcal{A} denotes the area over which deformation takes place. Thus, without dilation, mass conservation demands that the free surface descends exactly to the bottom of the roller ($h_b = 0$). Conversely, any dilation implies that the incoming granular surface lies below the roller ($h_b > 0$), for which there was no experimental evidence (if anything, the medium is compacted and the cylinders roll at a position below the incoming surface). The predicted free surfaces for the two values of dilation angle are also presented in Figure 13. The excessive dilation of the Mohr-Coulomb model with $\nu = \phi$ leads to an unphysical descent of the free surface, which is avoided by taking $\nu = 0$.

B. The cohesive Collins solution for $a \ll R$

For cohesive material without gravity, the $p \sin \phi$ factors in (3.9) are replaced by the cohesion c , and the slipline solution consists of a Rankine wedge leading a centred fan with circular

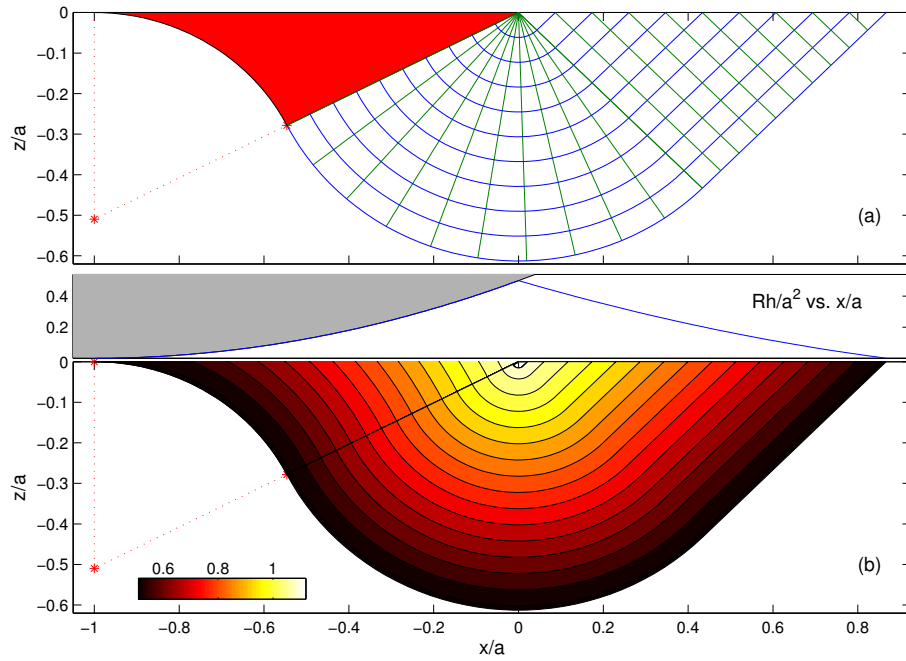


Figure 14: (a) Slipline field and (b) speed contours of the cohesive solution for $\psi_p = -17\pi/20$. The scaled free-surface shape $Rh(x)/a^2$ is also plotted in (b).

α -lines and straight radial β -lines. The fan geometry demands that the β -lines be straight everywhere, and so the rigidly rotating plug attached to the roller spans the entire contact area and $\ell = \tan \psi_p$; see Figure 14. Within the Rankine wedge the sliplines are inclined at $\pm \frac{1}{4}\pi$ to the horizontal, with $\theta = \frac{1}{2}\pi$ and $p = c$ ($\epsilon \equiv \frac{1}{4}\pi$). The fan extends back to the angle ψ_p from $\psi = -\frac{1}{4}\pi$, and within it, $\theta = \frac{3}{4}\pi + \psi$ and $p + 2c\theta = c(1 + \pi)$, or $p = c(1 - \frac{1}{2}\pi - 2\psi)$. Along the circular failure arc that continues the lowest α -line, $\theta = \frac{1}{4}\pi - \chi$ and $p + 2c\theta = c(1 + \pi)$, or $p = c(1 + \frac{1}{2}\pi + 2\chi)$, for $0 \leq \chi \leq -\psi_p - \frac{1}{2}\pi$. The force exerted on the roller can then be determined by integrating over the contour \mathcal{L} as in § 3. Again, there is a special value, $\ell = \ell_* \approx 0.43$, for which the horizontal force vanishes, leading to the lift force, $F_z \sim 4.90ac$, and rolling resistance, $F_r \sim 3.25a^2c/R$.

Within the yielded region, the velocity field is directed along the α -lines with speed $u_\alpha = -\Omega(r + a \sec \psi_p)$ (the velocity equations are $du_\alpha = -u_\beta d\theta$ and $du_\beta = u_\alpha d\theta$ along the two characteristics, and $u_\beta = 0$ along the lowest α -line, implying $u_\beta = 0$ everywhere); cf. Figure 14(b). The velocity at the free surface is therefore $\frac{1}{2}\sqrt{2}u_\alpha(1, 1) = -\frac{1}{2}\Omega(x + a\sqrt{2}\sec \psi_p)(1, 1)$, which implies the free surface profile from (A 4),

$$h(x) = \frac{a^2}{2R} + \frac{x}{4R}(x + 2a\sqrt{2}\sec \psi_p). \quad (\text{A } 1)$$

At the front of the bow wave, $x = x_f \equiv -a(\sec \psi_p + \tan \psi_p)\sqrt{2}$, we find $h = 0$, confirming that the bottom of the roller lies at the level of the undeformed surface; see Figure 14.

References

1. Bekker MG. 1969 *Introduction to terrain-vehicle systems*. University of Michigan Press.
2. Ding L, Gao H, Deng Z, Nagatani K, Yoshida K. 2011 Experimental study and analysis on driving wheels performance for planetary exploration rovers moving in deformable soil. *Journal of Terramechanics* **48**, 27–45.

3. Johnson JB, Kulchitsky AV, Duvoy P, Iagnemma K, Senatore C, Arvidson RE, Moore J. 2015 Discrete element method simulations of Mars Exploration Rover wheel performance. *Journal of Terramechanics* **62**, 31–40.
4. Kirkby M, Statham I. 1975 Surface stone movement and scree formation. *The Journal of Geology* **83**, 349–362.
5. Reynolds O. 1876 On rolling friction. *Philosophical Transactions of the Royal Society of London* **166**, 155–174.
6. Eldredge K, Tabor D. 1955 The mechanism of rolling friction. I. The plastic range. *Proceedings of the Royal Society of London A: Mathematical, Physical and Engineering Sciences* **229**, 181–198.
7. Kendall K. 1975 Rolling friction and adhesion between smooth solids. *Wear* **33**, 351–358.
8. Gee-Clough D. 1978 The effect of wheel width on the rolling resistance of rigid wheels in sand. *Journal of Terramechanics* **15**, 161–184.
9. Wong JY, Reece A. 1967a Prediction of rigid wheel performance based on the analysis of soil-wheel stresses part I. Performance of driven rigid wheels. *Journal of Terramechanics* **4**, 81–98.
10. Wong JY, Reece A. 1967b Prediction of rigid wheel performance based on the analysis of soil-wheel stresses: Part II. Performance of towed rigid wheels. *Journal of Terramechanics* **4**, 7–25.
11. Wong JY. 1967 Behaviour of soil beneath rigid wheels. *Journal of Agricultural Engineering Research* **12**, 257–269.
12. Wiendieck KW. 1968 A theoretical evaluation of the shear-to-normal stress ratio at the soil-wheel interface. *Journal of Terramechanics* **5**, 9–25.
13. Nowatzki E, Karafiath LL. 1974 General yield conditions in a plasticity analysis of soil-wheel interaction. *Journal of Terramechanics* **11**, 29–44.
14. Senatore C, Iagnemma K. 2014 Analysis of stress distributions under lightweight wheeled vehicles. *Journal of Terramechanics* **51**, 1–17.
15. Hambleton J, Drescher A. 2009 On modeling a rolling wheel in the presence of plastic deformation as a three-or two-dimensional process. *International Journal of Mechanical Sciences* **51**, 846–855.
16. Hambleton J, Stanier S. 2017 Predicting wheel forces using bearing capacity theory for general planar loads. *International Journal of Vehicle Performance* **3**, 71–88.
17. De Blasio FV, Saeter MB. 2009 Rolling friction on a granular medium. *Physical Review E* **79**, 022301.
18. Andreotti B, Forterre Y, Pouliquen O. 2013 *Granular media: between fluid and solid*. Cambridge University Press.
19. Spencer A. 1961 Perturbation methods in plasticity: I plane strain of non-homogeneous plastic solids. *Journal of the Mechanics and Physics of Solids* **9**, 279–288.
20. Spencer A. 1962 Perturbation methods in plasticity: III plane strain of ideal soils and plastic solids with body forces. *Journal of the Mechanics and Physics of Solids* **10**, 165–177.
21. Marshall EA. 1968 Rolling contact with plastic deformation. *Journal of the Mechanics and Physics of Solids* **16**, 243–254.
22. Tordesillas A, Shi J. 2000 The frictionless rolling contact of a rigid circular cylinder on a semi-infinite granular material. *Journal of engineering mathematics*.
23. Terzaghi K. 1943 *Theoretical soil mechanics*. Chapman And Hall Limited, London.
24. Salençon J. 1977 *Application of the theory of plasticity in soil mechanics*. John Wiley & Sons.
25. Martin C. 2005 Exact bearing capacity calculations using the method of characteristics. *Proc. IACMAG. Turin* pp. 441–450.
26. Collins I. 1978 Rolling of a rigid cylinder on a rigid-perfectly plastic half-space. *Journal de Mécanique appliquée* **2**, 431–448.
27. Petryk H. 1983 A slip-line field analysis of the rolling contact problem at high loads. *International journal of mechanical sciences* **25**, 265–275.
28. Sauret A, Balmforth NJ, Caulfield CP, McElwaine JN. 2014 Bulldozing of granular material. *Journal of Fluid Mechanics* **748**, 143–174.
29. Bradski G. 2000 Open Source Computer Vision Library. *Dr. Dobb's Journal of Software Tools*.
30. Drucker DC, Prager W. 1952 Soil mechanics and plastic analysis or limit design. *Quarterly of applied mathematics*.
31. Poorooshasb H, Holubec I, Sherbourne A. 1967 Yielding and flow of sand in triaxial compression: Parts II and III. *Canadian Geotechnical Journal* **4**, 376–397.
32. Roscoe KH. 1970 The influence of strains in soil mechanics. *Geotechnique* **20**, 129–170.